



Dual-branch residual network for lung nodule segmentation

Haichao Cao^a, Hong Liu^{a,*}, Enmin Song^a, Chih-Cheng Hung^b, Guangzhi Ma^a,
Xiangyang Xu^a, Renchao Jin^a, Jianguo Lu^a

^a Huazhong University of Science and Technology, School of Computer Science & Technology, Wuhan, 430074, China

^b Kennesaw State University, The Laboratory for Machine Vision and Security Research, 1000 Chastain Rd., Kennesaw, GA 30144, USA

ARTICLE INFO

Article history:

Received 4 May 2019

Received in revised form 10 October 2019

Accepted 8 November 2019

Available online 12 November 2019

Keywords:

Lung nodule segmentation

Residual neural networks

Deep learning

Computer-aided diagnosis

ABSTRACT

An accurate segmentation of lung nodules in computed tomography (CT) images is critical to lung cancer analysis and diagnosis. However, due to the variety of lung nodules and the similarity of visual characteristics between nodules and their surroundings, a robust segmentation of nodules becomes a challenging problem. In this study, we propose the Dual-branch Residual Network (DB-ResNet) which is a data-driven model. Our approach integrates two new schemes to improve the generalization capability of the model: (1) the proposed model can simultaneously capture multi-view and multi-scale features of different nodules in CT images; (2) we combine the features of the intensity and the convolutional neural networks (CNN). We propose a pooling method, called the central intensity-pooling layer (CIP), to extract the intensity features of the center voxel of the block, and then use the CNN to obtain the convolutional features of the center voxel of the block. In addition, we designed a weighted sampling strategy based on the boundary of nodules for the selection of those voxels using the weighting score, to increase the accuracy of the model. The proposed method has been extensively evaluated on the LIDC-IDRI dataset containing 986 nodules. Experimental results show that the DB-ResNet achieves superior segmentation performance with the dice similarity coefficient (DSC) of 82.74% on the dataset. Moreover, we compared our results with those of four radiologists on the same dataset. The comparison showed that our DSC was 0.49% higher than that of human experts. This proves that our proposed method is as good as the experienced radiologist.

© 2019 Elsevier B.V. All rights reserved.

1. Introduction

Lung cancer is a relatively common and deadly cancer with a five-year survival rate of only 18% [1]. The use of computed tomography (CT) images for treatment, monitoring, and analysis is an important strategy for early lung cancer diagnosis and survival time improvement [2]. With this technique, the accurate segmentation of lung nodules is important because it can directly affect the subsequent analysis results [3]. Due to the fact that the number of CT images is increasing, the development of a robust automatic segmentation model has important clinical significance for avoiding tedious manual treatment and reducing the diagnostic difference among doctors [4].

Due to the heterogeneity of lung nodules on CT images (as shown in Fig. 1), it has been difficult to obtain an accurate segmentation performance [5–7]. Specifically, the similarity of visual characteristics between nodules and their surroundings causes the difficulty for the segmentation. In particular, the juxtapleural nodules (Fig. 1(b)), because its intensity is very similar to the lung

wall, makes it difficult to segment such nodules using conventional methods. It is also difficult to segment the juxtavascular nodules (Fig. 1(c)) because it is connected to blood vessels in the lung parenchyma and its low contrast compared with blood vessels. A similar situation is the ground-glass opacity (GGO, Fig. 1(f)) nodules, due to its low contrast to the surrounding background, result in simple threshold- and morphological-based methods which cannot handle such nodules. In addition, for calcific nodules (Fig. 1(e)), because of the high contrast with surrounding pixels, a simple threshold segmentation method (for example, OTSU algorithm) can segment such nodules well, but such a threshold method cannot be applied to both the adhesion-type nodules (juxtapleural and juxtavascular) and the GGO nodules. It is a challenge for a segmentation method to be adapted to these three types of nodules simultaneously. Fig. 1(d) shows a cavitory nodule in which the cavity is an important indication of the malignant nodule. In the CT image, this type of nodule is a round air-like low-density shadow greater than 5 mm in the lesion. Since the density of the low-density shadows in the cavitory nodules differs greatly from that of other parts of the body, it is also a challenge to accurately segment such nodules [8]. It should be pointed out that there exist some nodules with small

* Corresponding author.

E-mail address: hl.cbib@gmail.com (H. Liu).

diameters in the lungs as shown in Fig. 1(g). These nodules are very similar to the intensity of the surrounding noise, which makes these nodules more difficult to be distinguished. Besides, the existence of such small nodules largely limits the capability of downsampling of the segmentation network. In other words, the network cannot extract deeper semantic features, which will greatly affect the efficiency of the feature extraction of large nodules. Therefore, it is essential on how to design a segmentation network to accommodate the multi-scale problem of nodules.

The intensity-based method using morphological operations [9,10] and region growing [5,11] were used for lung nodule segmentation. In addition, energy-optimized methods such as graph cut [12] and level set [7] have also been used. However, both approaches are not robust for segmenting juxtaleural nodules and small nodules with a diameter of less than 6 mm. For example, in a morphology-based method, the size of the morphological template is difficult to be adaptive for the nodules of various diameters [5]. Some effective measures are semi-automatic interaction methods that require user intervention [13] and shape-constrained methods based on specific rules [7,14]. However, this method may fail for irregular nodules due to the violation of shape assumption. The limitations of segmentation directly using raw gray values indicate that a robust method for segmentation of lung nodules is urgently needed.

In recent years, convolutional neural networks (CNN) have been demonstrated their strength in various competitions, which undoubtedly become the mainstream architecture in the field of computer vision [15–17]. An important reason for this is that CNN can automatically extract features from the convolutional layer and implicitly learn from the training data without artificially designing relevant features based on the prior knowledge [18]. CNN have also given exciting results in medical image segmentation tasks [19–21]. However, it should be pointed out that the lung nodules with large differences in the size, morphology, and contrast with surrounding tissues (as shown in Fig. 1), the current segmentation methods for lung nodules using CNN are still immature. Therefore, it is necessary to explore more advanced models and algorithms for the development of lung nodules segmentation methods based on CNN.

To adapt to the heterogeneity of lung nodules, we followed the voxel classification scheme and proposed a Dual-Branch Residual Network (DB-ResNet), which is suitable for various types of lung nodule segmentation. In general, our technical contributions in this work have the following four aspects.

(1) For small nodules and juxtaleural nodules, the proposed DB-ResNet model can achieve attractive segmentation performance as shown in Table 5.

(2) A Dual-branch CNN architecture based on ResNet is proposed in which the extracted multi-view and multi-scale features are used to classify each voxel (Section 3.1.2). In this architecture, multi-view branches are used to model the upper, middle, and lower slices while the multi-scale branches are used to model the three different scales of the middle slice (Fig. 2).

(3) We proposed a central intensity-pooling layer that preserves the intensity features centered on the target voxel rather than the intensity information at the boundary. We incorporate the traditional intensity features into the CNN architecture to achieve a performance improvement in the nodule segmentation model (Section 3.1.3).

(4) The weighted sampling strategy [22] was improved to handle the unbalanced training labels to achieve efficient model training. In this improved sampling strategy, the small nodules can be adequately sampled based on the number of voxels located at the boundary of the nodules (Section 3.2).

2. Related work

In recent years, many methods for segmentation of lung nodules have been proposed, such as morphological based methods, region growing based methods, energy based optimization methods, and machine learning based methods. Below we will further describe these four types of methods.

In the morphological method, in order to remove the nodule-attached vessels, morphological operations were applied and lung nodules were then isolated according to the selection of connected regions [23]. Furthermore, in order to better separate the lung wall from the juxtaleural nodules, a morphological operation combining the shape hypothesis was introduced to replace the fixed-size morphological template [24,25]. In general, the segmentation of nodules is very challenging by using the morphological operations [9].

At present, most region growing methods are only well adapted to isolate calcified nodules but not able to segment the juxtaleural nodules and the juxtaleural nodules [5]. To alleviate this problem, Dehmeshki et al. proposed a new region growing method based on intensity information, distance, fuzzy connectivity and peripheral contrast [11]. Although they introduced a variety of rules which are still not adapted well to irregularly shaped nodules because this type of nodules has almost no rules to follow.

In the energy optimization method, researchers usually convert the segmentation task into an energy minimization task for processing. For example, in [26–29], the author uses a level set function to characterize the image, and when the segmented contour matches the nodule boundary, the energy function reaches a minimum. A similar approach is the lung nodules segmentation method based on shape prior hypotheses and level sets proposed by Farag et al. [7]. In addition, the graph-cut method that converts the lung nodule segmentation task into the maximum flow problem is also used [12,30,31]. However, these methods are not well adapted to the GGO nodules and the juxtaleural nodules.

In the machine learning method, in order to segment the target, related features need to be designed and extracted for subsequent voxel classification [32–35]. For example, Lu et al. designed a set of features with translational and rotational invariance for the classification [36]. Wu et al. proposed a method for segmentation of lung nodules based on conditional random fields, which can extract the texture and shape features of nodules [37]. Hu et al. segmented the lungs and then performed vascular feature extraction based on the Hessian matrix to obtain the mask of the lung blood vessels. The blood vessels are then removed from the lung mask and the artificial neural networks are used for the classification [38]. Besides, there is a method for segmentation of the ground-glass nodules based on asymmetric multi-phase deformable models proposed by Jung et al. [39]. According to the Hessian strategy, a 3D multiscale lung nodule segmentation method was proposed by Gonçalves et al. [40].

CNN is a multi-layer neural network designed to learn the hierarchical mapping between raw image data and labels [41, 42]. For the CNN-based lung nodule segmentation method, similar to the previous machine learning-based method, it is also solved by converting the segmentation task into a voxel classification problem. For example, Wang et al. proposed a multi-view convolutional neural network (MV-CNN) for the segmentation of lung nodules. The MV-CNN consists of three CNN branches, which correspond to three views of the axial plane, the coronal plane and the sagittal plane [43]. Later, Wang et al. proposed a semi-automatic central focused CNN [22] for voxels classification, however, the model is not ideal for small nodules. To better segment the lung nodules, Zhao et al. proposed an improved pyramid deconvolution neural network. The segmentation architecture

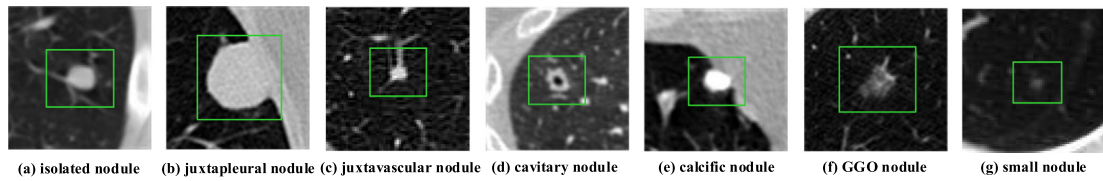


Fig. 1. Example images of a heterogeneous lung nodule in CT images. Note that GGO in sub-figure (f) represents a ground-glass opacity nodule, and (g) is a small nodule having a diameter of less than 4.4 mm.

effectively combines high-level semantic features with low-level fine-grained features [44]. Huang et al. proposed a fully automated method for segmentation of lung nodules, which is divided into four steps, namely, detection of candidate nodules, candidate merging, false positive reduction, and nodule segmentation [45]. On the other hand, fully convolutional networks (FCN) [46] is another approach of image segmentation. For example, the 2D UNet network architecture proposed by Ronneberger et al. [47] and the 3D UNet network architecture proposed by Çiçek et al. [48] are a kind of segmentation methods that can better adapt to medical images.

3. Our proposed method

We will describe our proposed method in detail below. The method is divided into three components: (1) the model architecture, (2) the sampling strategy, and (3) the post-processing approach.

3.1. The model architecture

The proposed DB-ResNet model utilizes three longitudinal views (three contiguous slices) and three transversal scales to segment the lung nodules. Given a voxel in a slice of the CT images, we extract multiple views from the slices centered in the current voxel and multiple different size of patches as multiple scales. In this study, we limit the multiple views and scales to three views and scales. Three views are taken from the previous, current and next slices. Since the proposed lung nodule segmentation method is based on the 2D CNN network architecture, the input data patch containing three slices is sufficient to fit different size nodules. The multiple views and scales will be used as input, and then output the probability that this voxel belongs to the nodule. Fig. 2 shows the proposed architecture of DB-ResNet. Table 1 shows the corresponding network parameters.

3.1.1. Network structure

The network contains two deep branches that share the same structure, but the inputs used for training are different. Each branch of the proposed network architecture contains 32 convolutional layers, two central pooling layers [22], one central intensity-pooling (CIP) layer (see Section 3.1.3 for a detailed description) and one shared fully-connected layer. The 32 convolution layers in the CNN are divided into three categories: the first is a ConvBlock consisting of two convolutional layers, the second is a ResBlock cluster consisting of four residual blocks [49], and the last is a ResBlock cluster consisting of six residual blocks. To speed up the training process, each convolutional layer is batch-normalized to normalize the corresponding output [50]. After each convolution layer, a parametric rectified linear unit (PRELU) is used as a nonlinear activation function [51].

We use the average pooling (Fig. 2, AP) for the output of the last convolutional layer of each branch. The output of the average pooling is then concatenated with the output of the CIP layer to fuse the depth features produced by the convolution layer and the intensity features generated by the CIP layer. At the end of the

model layers, the features generated by the two CNN branches are combined with the concatenation, and the concatenated results are then connected to a fully-connected layer to capture the correlation of the features generated by the two CNN branches.

The parameters of the DB-ResNet network architecture shown in Fig. 2 are listed in Table 1. Among them, the convolution kernel size, the number of output channels and the number of stacked blocks of ConvBlock_x, ResBlock1_x and ResBlock2_x in DB-ResNet32 are set with reference to conv1, conv3_x, and conv4_x in ResNet50. DB-ResNet83, DB-ResNet134 is similar to DB-ResNet32, which are parameter settings made with reference to ResNet101 and ResNet152, respectively. Please note that the reason for changing conv1 (7*7, 64) in ResNet to two (3*3, 32) is to reduce the model parameters. And according to our experiments, changing the number of output channels 64 of ConvBlock_x to 32 has little effect on the final segmentation performance.

The goal of network training is to maximize the probability of the correct class for each voxel. We achieve this by minimizing the cross-entropy loss of each training sample. For a given input patch belonging to {0, 1}, assuming that y_n is a true label, then the loss function is defined as shown in Eq. (1):

$$L = -\frac{1}{N} \sum_{n=1}^N [y_n \log(y'_n) + (1 - y_n) \log(1 - y'_n)] \quad (1)$$

Where y'_n represents the prediction probability of the DB-ResNet, and N is the number of samples.

In the experiment, we used the Stochastic Gradient Descent (SGD) algorithm [52] as a model update method. The SGD optimizer has several parameter settings: the initial learning rate is 0.001, and then the learning rate is decreased by ten percent in every five epochs. In addition, the momentum setting is 0.9. However, due to the limitation of GPU memory, only a batch size of 32 samples are used. To avoid overfitting during the training process, we adopted the early stopping training strategy [53].

3.1.2. Dual-branch architecture

The proposed dual-branch residual network (DB-ResNet) architecture aims to capture both multi-view features in multiple slices and multi-scale features in the current slice.

The input size of the multi-view branch is a $3 \times 35 \times 35$ 3D data patch. Specifically, for a voxel, we extend the current, previous, and subsequent slices centered on this voxel to extract training patches (see Fig. 2, Multi-view Branch). This three-slice patch extracted are treated as three channel images and fed to the multi-view CNN branch.

Simultaneously, we have introduced a multi-scale branch trying to focus on learning features from the current slice because of their high resolution in all CT scans. The purpose of designing multi-scale branches is to model the relationship among three-scale patches through the feature extraction layer. Firstly, three image patches with a size of 65×65 , 50×50 and 35×35 , respectively, were extracted from the slice in which the target voxel is located. They are then rescaled to the same size of 35×35 using a third-order spline interpolation and forming

Table 1

Network parameters of the DB-ResNet. Building blocks are shown in brackets with the numbers of blocks stacked. Downsampling is performed using Central Pooling before the first layer of ResBlock1_x and ResBlock2_x.

Layer name	Output size	32-Layer	83-Layer	134-Layer
ConvBlock_x	35×35	$[3 \times 3, 32] \times 2$	$[3 \times 3, 32] \times 2$	$[3 \times 3, 32] \times 2$
ResBlock1_x	17×17	$\begin{bmatrix} 1 \times 1, 128 \\ 3 \times 3, 128 \\ 1 \times 1, 512 \end{bmatrix} \times 4$	$\begin{bmatrix} 1 \times 1, 128 \\ 3 \times 3, 128 \\ 1 \times 1, 512 \end{bmatrix} \times 4$	$\begin{bmatrix} 1 \times 1, 128 \\ 3 \times 3, 128 \\ 1 \times 1, 512 \end{bmatrix} \times 8$
ResBlock2_x	8×8	$\begin{bmatrix} 1 \times 1, 256 \\ 3 \times 3, 256 \\ 1 \times 1, 1024 \end{bmatrix} \times 6$	$\begin{bmatrix} 1 \times 1, 256 \\ 3 \times 3, 256 \\ 1 \times 1, 1024 \end{bmatrix} \times 23$	$\begin{bmatrix} 1 \times 1, 256 \\ 3 \times 3, 256 \\ 1 \times 1, 1024 \end{bmatrix} \times 36$
	1×1	Average Pooling, Concatenate, 2-d fc, softmax		
Params		0.68×10^7	2.3×10^7	3.7×10^7

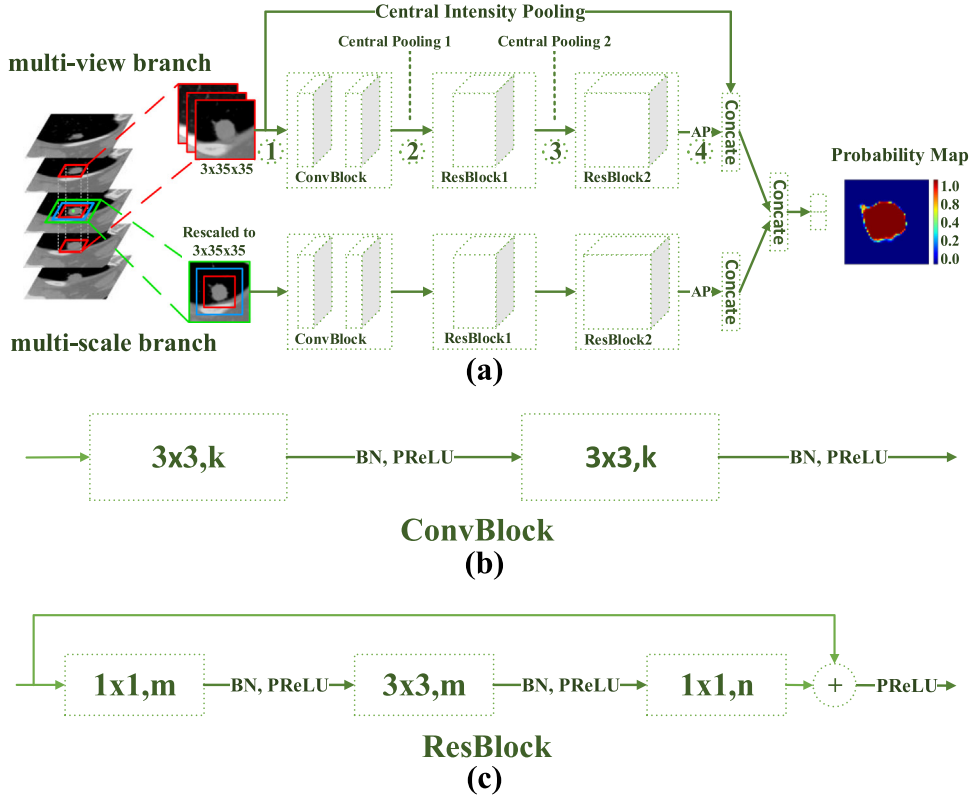


Fig. 2. (a) Illustration of the proposed DB-ResNet architecture where AP and Concat represent the Average Pooling operation and Concatenate operation, respectively. The symbol $\cdot N$ indicates where the Central Intensity-Pooling can be placed, (b) the diagram of the convolution block (ConvBlock), and (c) the diagram of the residual block (ResBlock). The parameters k, m and n indicate the number of channels.

three-channel patches as input to a multi-scale CNN branch (see Fig. 2, multi-scale branch).

In addition, in order to further improve the segmentation performance, we also integrate the residual learning structure into the network. Moreover, we use the bottleneck structure where the head and end are 1×1 convolutions (to reduce and restore dimensions) and the middle is a 3×3 convolution, replacing the original residual learning structure, which can reduce network parameters and increase network depth [49].

The motivation for designing a multi-view branch is to adapt to the segmentation of the three-dimensional object. Specifically, since the lung nodule is a three-dimensional object, the data block input to the model needs to contain certain spatial information, so that the model can learn the location relationship between the slices. However, since a 2D segmentation network is proposed, multi-view branches are needed to meet this need.

The motivation for designing multi-scale branches is to adapt to changes in the size of the lung nodules. Fig. 3 shows the size

distribution of the nodules. The small scale 35×35 in the multi-scale branch is mainly used to adapt to nodules less than 15 mm in size (about 80% of the total number of nodules). The other two large scales, 50×50 and 65×65 , are used to adapt to the remaining 20% of the large nodules, providing them with richer contextual information.

3.1.3. The central intensity-pooling

The conventional segmentation method usually utilizes the intensity information of the target. For the segmentation of nodules, we can also use the same information. In particular, for isolated nodules and calcified nodules, the intensity information is useful due to a large contrast between the nodules and the surrounding background. Therefore, we designed a pooling layer that calculates either the center position of the feature map or its surrounding intensity information.

Fig. 4 shows the central intensity-pooling process for three different pooling kernel sizes. Among them, the yellow mark

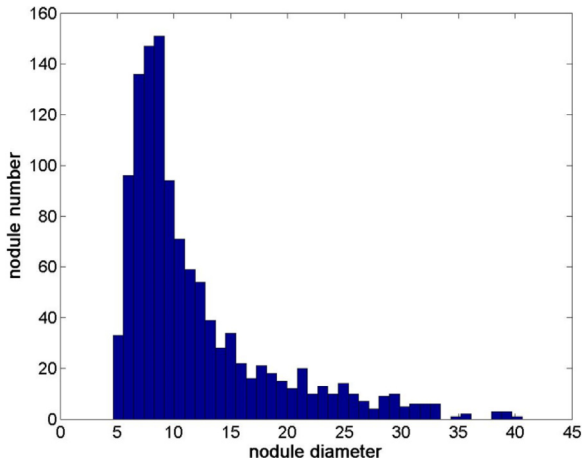


Fig. 3. A distribution of the sizes of lung nodules.

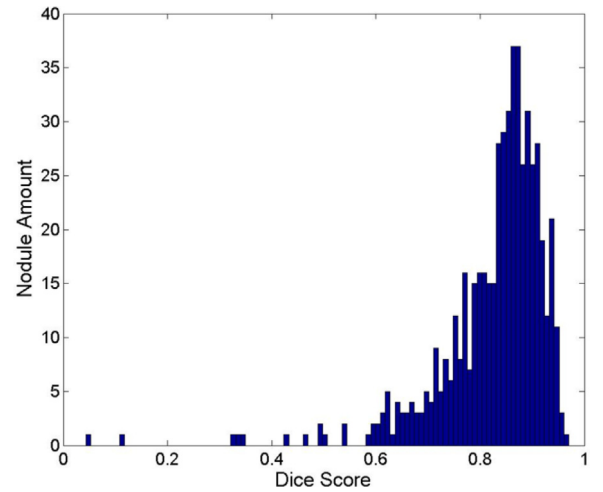


Fig. 5. DSC distributions of the LIDC-IDRI testing set.

corresponds to a pooling process with a pooling kernel size of 1×1 , and the result is the intensity value of the pixel in the center of the input image. The blue mark corresponds to the pooling process with a pooling kernel size of 3×3 , and the result is the average intensity value of the surrounding 3×3 region centered on the center pixel of the input image. The corresponding pooling process for the red mark is similar to the blue mark. In practice, we designed two different sizes of the pooling kernel. One is a smaller local pooling kernel that can obtain local intensity information at the center of the image; the other is a larger global pooling kernel that can obtain richer contextual information. Since we predict the category of the center voxel of the patch, the proposed central intensity-pooling helps to extract the intensity features at the center of the patch.

This central intensity-pooling consists of two parameters: (1) the size of the different pooling kernel and (2) the number of pooling kernels for each type. As mentioned earlier, in this study, we have introduced two different sizes of the pooling kernel, and the number of pooling kernel for each type has only one. These two types correspond to the local pooling kernel and the global pooling kernel.

In our experiment, the size of the local pooling kernel is 1×1 , and the size of the global pooling kernel is 3×3 . The purpose of our choice of 1×1 size pooling kernel is to preserve the intensity value of the current voxel point. Experimental results show that this size of the pooling kernel is necessary. The purpose

of selecting a 3×3 size pooling kernel is to obtain richer context information to better reflect the intensity feature of the current voxel.

It should still be pointed out that the dominant feature used for classification is the depth feature of CNN learning, while the intensity feature is only used for assistance. Therefore, the proposed central intensity pooling will not affect the segmentation performance of partly-solid, irregular, cavitory nodules, etc.

3.2. The weighted sampling strategy

Since our approach focuses on automatically learning advanced semantic features from images, a large number of voxel patches are needed as training samples to improve the accuracy of the model. However, in a CT slice, the ratio of nodule to non-nodular voxel is generally 1:370 ($\pi r^2 : S - \pi r^2$, where $r=15$ is the maximum radius of the nodule and $S = 512^2$ is the area of each slice), which is a highly data imbalance problem. If a traditional random sampling is used, this will lead to a trained model that is biased towards the non-nodal classes. Therefore, in order to avoid this problem, we use a weighted sampling strategy [22]. However, our experimental results have found that this weighted sampling strategy has poor sampling results for small nodules with a diameter of less than 6 mm.

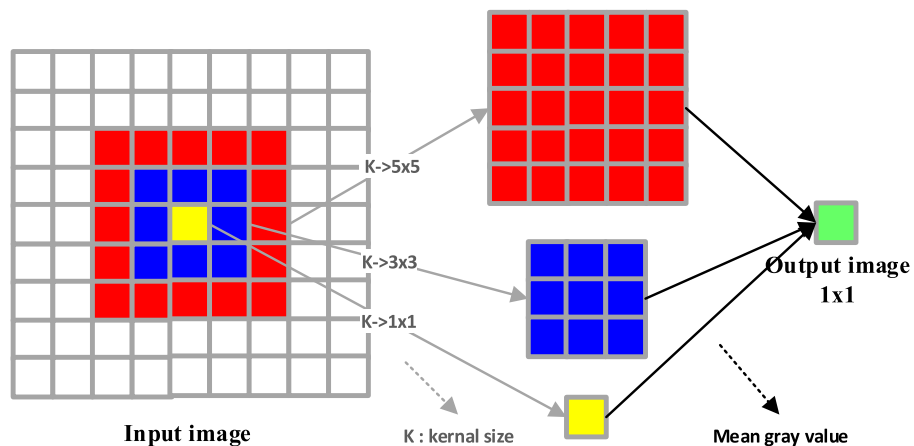


Fig. 4. A central intensity-pooling process: this shows the processing of three different pooling kernel sizes, corresponding to the red, blue, and yellow, and the sizes are 5×5 , 3×3 , and 1×1 , respectively.

Table 2

The data distribution of the LIDC-IDRI dataset training, validation and testing sets. Among them, the values are displayed in the format of mean \pm standard deviation.

Characteristics	Training set (n = 387)	Validation set (n = 55)	Test set (n = 544)
Diameter (mm)	8.34 \pm 4.73	8.17 \pm 4.61	7.90 \pm 4.14
Sphericity	3.80 \pm 0.58	3.84 \pm 0.62	3.85 \pm 0.58
Margin	4.07 \pm 0.73	4.06 \pm 0.81	4.11 \pm 0.78
Spiculation	1.61 \pm 0.78	1.54 \pm 0.69	1.57 \pm 0.74
Texture	4.56 \pm 0.83	4.45 \pm 0.98	4.57 \pm 0.80
Calcification	5.65 \pm 0.80	5.68 \pm 0.77	5.67 \pm 0.80
Internal structure	1.01 \pm 0.16	1.03 \pm 0.20	1.01 \pm 0.08
Lobulation	1.74 \pm 0.72	1.75 \pm 0.74	1.69 \pm 0.71
Subtlety	4.00 \pm 0.78	3.89 \pm 0.74	3.95 \pm 0.75
Malignancy	2.95 \pm 0.91	2.87 \pm 0.77	2.91 \pm 0.91

Note: The range of all characteristic values except diameter, internal structure and calcification is 1–5, wherein the internal structure and calcification range from 1 to 4, 1 to 6, respectively. Margin indicates the clarity of the nodule edge. Lobulation and spiculation indicate the number of these shapes. Texture is a statistic of the distribution properties of the local gray information of nodules. Internal structural represents the internal composition of the nodule. Malignancy, calcification, and Sphericity indicate the possibility that the nodule is such a feature. Subtlety describes the contrast of the nodule region and its surrounding region. There were no significant statistical differences in the characteristics of the three subsets.

To elaborate further on the above issue, we assume that the nodules in each slice are circular, and the nodule diameter of the k th slice is R . Then, the total number of nodule voxels and nodule voxels at the boundary in the k th slice can be approximated as $\pi R^2/4$ and πR , respectively. According to the original weighted sampling method, only 40% of the total number of nodal voxels is sampled. If R is less than 10, the number of sampling points of the nodule class will be smaller than the number of the voxels sampled at the boundary. In our experiment, we found that if a nodule is less than 6 mm in diameter, it will have almost half of the voxels at their boundary are not sampled.

To solve the problem of insufficient number of samples for small nodules, we set the number of nodule samples to twice the number of voxels at the nodule boundary. Simultaneously, we also ensure that the number of non-nodule samples is the same as the number of nodule samples. It should be noted that for small nodules that are less than 6 mm in diameter, the total number of nodule voxels might be less than twice the number of boundary voxels. In this case, we will take all the voxels of such small nodules to improve the generalization capability of the model for such small nodules. Experimental results have shown that this improved sampling strategy increases the DSC from 78.89% to 80.30%. The detailed results are given in Table 3 of Section 5.1.

3.3. Post-processing

Since the method proposed in this paper is a semi-automatic segmentation model, it is necessary to give the volume of interest (VOI) where the nodule is located before segmentation. However, since the nodules are usually distributed over multiple CT slices, it is tedious to manually specify the region of interest (ROI) in which the nodules are located, layer-by-layer. To facilitate the doctor's operation, we performed the following post-processing operation, that is, it is only necessary to manually designate a bounding box called a starting slice on one CT slice.

Then repeat applying the same bounding box to the previous and next slices until the following experimental conditions are satisfied: The nodule intersection area of the current slice and the previous slice is less than 30% of the nodule area in the previous slice.

To remove the noisy voxels, we made a simple connected region selection as follows: (1) When noise appears in the starting slice, we select the isolated region closest to the center of the bounding box, and (2) when noise occurs in other slices, we choose the connected region where the overlap $O=V(Gt \cap Seg)/V(Gt \cup Seg)$ (will be explained in detail in Section 4.2) of the current slice and the previous slice nodule mask is the largest.

4. Data and experiments

We give the information of the dataset and experiments in detail in this section. The evaluation criteria are described below.

4.1. Data

We used public datasets from the Lung Image Database Consortium and Image Database Resource Initiative (LIDC-IDRI) in our experiments and for comparison [54–56]. In this study, we studied all 986 nodule samples labeled by four radiologists in the LIDC-IDRI dataset. The motivation is to ensure the accuracy of the gold standard, because the nodules marked by the four doctors are most likely to be true nodules. Due to the differences in labeling between the four radiologists, the 50% consistency criterion [5] was used to generate the ground-truth boundary. That is, if the current voxel point is marked by two or more physicians, the voxel point will be preserved. Otherwise, it will be removed from the gold standard.

We randomly partitioned 986 nodules into three subsets for training, validation, and testing with the number of nodules contained in each subset was 387, 55, and 544, respectively. As shown in Table 2, the clinical characteristics of the three subsets have a similar statistical distribution.

Table 3

Ablation study on LIDC-IDRI testing dataset. Note that Scale represents the 50*50 size of the multi-scale branch; BWS represents a weighted sampling strategy based on the boundary points; DB represents dual-branch architecture; ResNet represents the residual network, see Table 1; MV-ResNet32 represents an independent multi-view branch; MS-ResNet32 represents an independent multi-scale branch; CIP_N denotes adding a central intensity-pooling layer from the first to the Nth position; Post indicates the proposed post-processing operation.

Method	DSC (%)	ASD (mm)	SEN (%)	PPV (%)
CF-CNN	78.55 \pm 12.49	0.27 \pm 0.35	86.01 \pm 15.22	75.79 \pm 14.73
CF-CNN + Scale	78.89 \pm 11.67	0.26 \pm 0.29	86.21 \pm 14.66	75.95 \pm 14.41
CF-CNN + Scale + BWS	80.30 \pm 11.34	0.26 \pm 0.45	85.40 \pm 13.27	78.69 \pm 14.49
MV-ResNet32	81.90 \pm 09.52	0.23 \pm 0.28	88.18 \pm 12.04	78.23 \pm 12.69
MS-ResNet32	81.55 \pm 11.65	0.24 \pm 0.38	84.89 \pm 15.14	81.66 \pm 13.86
DB-ResNet32	82.37 \pm 10.98	0.22 \pm 0.34	88.36 \pm 13.09	79.58 \pm 13.30
DB-ResNet83	81.33 \pm 11.69	0.24 \pm 0.39	86.94 \pm 14.42	79.33 \pm 14.08
DB-ResNet134	79.56 \pm 11.28	0.25 \pm 0.36	87.92 \pm 13.24	75.35 \pm 14.66
DB-ResNet32 + CIP_1	82.54 \pm 10.20	0.19 \pm 0.21	89.06 \pm 11.79	79.17 \pm 13.31
DB-ResNet32 + CIP_2	82.69 \pm 10.46	0.21 \pm 0.30	88.69 \pm 12.18	79.62 \pm 13.29
DB-ResNet32 + CIP_3	81.67 \pm 10.46	0.21 \pm 0.25	88.93 \pm 12.32	77.94 \pm 13.68
DB-ResNet32 + CIP_4	80.52 \pm 11.45	0.23 \pm 0.37	88.89 \pm 12.89	76.14 \pm 14.97
DB-ResNet32 + CIP_1 + Post	82.74 \pm 10.19	0.19 \pm 0.21	89.35 \pm 11.79	79.64 \pm 13.34

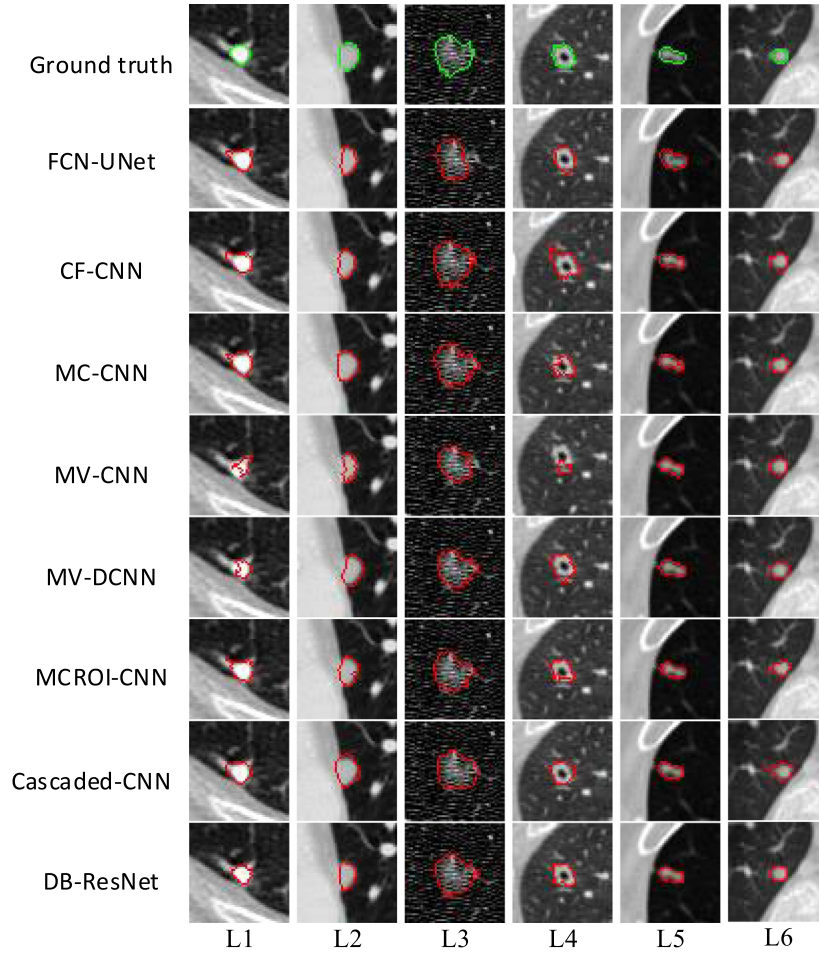


Fig. 6. A visual comparison of the segmentation results. From top to bottom: the ground truth of nodule, segmentation result of CF-CNN, MC-CNN, MV-CNN, MV-DCNN, MCROI-CNN, Cascaded-CNN, and DB-ResNet. Notations L1 to L6 are nodules of different types from the LIDC-IDRI testing set.

4.2. Evaluation criteria

To evaluate the segmentation results of the DB-ResNet model, we used the average surface distance (ASD) and dice similarity coefficient (DSC) as the primary evaluation criteria. DSC is a metric that is widely used to measure the overlap between two segmentation results [20,57]. To ensure the robustness of the evaluation, we also use the positive prediction value (PPV) and sensitivity (SEN) as auxiliary evaluation parameters. The entire definition is shown in formulae (2)–(5).

$$DSC = \frac{2 \times V(Gt \cap Seg)}{V(Gt) + V(Seg)} \quad (2)$$

$$ASD = \frac{1}{2} (mean_{i \in Gt} \min_{j \in Seg} d(i, j) + mean_{i \in Seg} \min_{j \in Gt} d(i, j)) \quad (3)$$

$$SEN = \frac{V(Gt \cap Seg)}{V(Gt)} \quad (4)$$

$$PPV = \frac{V(Gt \cap Seg)}{V(Seg)} \quad (5)$$

where “Gt” represents the result of expert labeling; “Seg” represents the segmentation result of DB-ResNet model. V represents the volume size calculated in voxel units and $d(i, j)$ represents the Euclidean distance between the voxel i and voxel j measured in millimeters.

4.3. The detail of implementation

In the experiment, we used a weighted sampling strategy (Section 3.2) to sample 0.47 million voxel patches extracted from the LIDC-IDRI training set. To avoid overfitting, we used a training strategy for early stopping: if there is no more improvement in performance, it will stop in an extra training with 10 epochs. It has been found through experiments that the DB-ResNet model generally stops around the 16th epoch, so we set the upper limit of the training epoch to 20. Our experiment is based on the Keras deep learning framework and the coding language is Python 3.6. Our experiment was carried out on a server equipped with an Intel Xeon processor and 125GB memory. In the model training, acceleration is performed on the NVIDIA GTX-1080Ti GPU (11GB video memory), and the DB-ResNet model takes about 31 h to converge.

5. Results and discussion

We give the ablation study of the proposed method, the overall performance of our method, and the experimental comparison with other methods below.

5.1. Ablation study

To verify the effectiveness of each component in the DB-ResNet architecture, we designed an ablation experiment based on the CF-CNN network architecture [22]. The relevant experimental results are shown in Table 3.

(1) Effect of Boundary-based Weighted Sampling (BWS)

In Table 3, CF-CNN + Scale indicates that we added a 50×50 scale to the 2-D branch of CF-CNN and then combined it with two scales of 65×65 and 35×35 to form our multi-scale branch. The DSC obtained by CF-CNN + Scale is 78.89%, which is slightly higher than that of CF-CNN. Then, based on CF-CNN + Scale, a weighted sampling strategy based on the boundary points is applied, and the DSC obtained is 80.30%. Compared to CF-CNN + Scale, its performance has improved by nearly 1.5%, which verifies the effectiveness of the boundary-based weighted sampling strategy.

(2) Effect of Residual Network

In Table 3, based on CF-CNN + Scale + BWS, DB-ResNet32 replaces two convolution blocks with two residual blocks. At this time, the DSC is 82.37%, which is an increased performance of two percent compared to the previous 80.30%. This proves the effectiveness of the residual block. Then, based on the ideas of ResNet101 and ResNet152 [49], we improve the network performance by increasing the depth of the network, but according to the results of the sixth and seventh rows in Table 3, it does not achieve what we expected. This may be due to the excessive complexity of the network, which leads to overfitting of the model.

In addition, the main difference between DB-ResNet and ResNet is that DB-ResNet consists of two branches, a multi-view branch, and a multi-scale branch. The two branches share the same network structure. In addition, in terms of network depth, the DB-ResNet architecture is only downsampled twice due to the small size of the lung nodules. It can be seen from the experimental results that the MV-ResNet32 and MS-ResNet32 cannot achieve the effect of DB-ResNet32. Among them, MV-ResNet32 and MS-ResNet32 represent an independent multi-view branch and an independent multi-scale branch. This proves to some extent that the proposed DB-ResNet architecture is superior to the existing ResNet architecture for lung nodule segmentation tasks.

(3) Effect of Central Intensity-Pooling

Based on DB-ResNet32, we integrated the proposed central intensity-pooling layer into DB-ResNet32. To verify the effectiveness of the central intensity-pooling layer, we performed four experiments, corresponding to rows 8–11 in Table 3. By comparing these four rows, we can see that DB-ResNet32 + CIP_1 is the best with an ASD of 0.19, which is an improvement of three percent over DB-ResNet32. For the other three performance indicators, both the DSC and the SEN are increased except the PPV is decreased by 0.41%. For the reason why the performance of DB-ResNet32 + CIP_3 and DB-ResNet32 + CIP_4 decline more obviously, our opinion is that the features used for classification, the proportion of traditional intensity features is increasing, even exceeding the deep convolutional features. This is unreasonable because the deep convolution feature in our network is crucial. Specifically, for DB-ResNet32 + CIP_3, the ratio of intensity features to convolution features is 584:1024, and the ratio for DB-ResNet32 + CIP_4 is 1608:1024.

(4) Effect of Post-processing

Finally, we verified the effectiveness of the proposed post-processing method. By comparing the ninth row and the last row in Table 3, it can be seen that although the performance is not significantly improved, the four performance measures are improved.

5.2. Overall performance

To better observe the performance of the proposed method in the testing set, we plot the histogram between the DSC value and the number of nodules, based on all samples in the testing set, as

Table 4

Mean DSCs (%) of consistency comparison between DB-ResNet and each radiologist, where R1 to R4 represent four radiologists.

	R1	R2	R3	R4	Average
R1	–	82.61	82.47	82.49	82.66 ± 0.48
R2	82.61	–	83.72	82.36	
R3	82.47	83.72	–	82.32	
R4	82.49	82.36	82.32	–	
DB-ResNet	82.32	84.02	82.94	83.30	83.15 ± 0.62

shown in Fig. 5. By observing Fig. 5, we can easily conclude that most of the nodules have a DSC value higher than 0.8.

To see if the segmentation results of our proposed method are comparable to those hand-labeled by human experts, we performed a consistency comparison between DB-ResNet and four radiologists, as shown in Table 4. Our results show that the stability of DB-ResNet is slightly weaker than that of four different radiologists. However, the DSC between DB-ResNet and each radiologist is 83.15% on average, which is higher than the average of 82.66% among inter-radiologists.

Further, we have collated the evaluation results of challenging small nodules and attached nodules. The relevant results are shown in Table 5. According to the experimental results in Table 5, it can be seen that the potential robust segmentation of the DB-ResNet is independent of the type of nodules and the size of nodules.

5.3. Experimental comparison

To illustrate the efficiency of the proposed method, we compared the results with other methods. Two different comparisons are provided: (1) a comparison with various different types of segmentation methods recently proposed and (2) a comparison of methods with the same segmentation architecture but different basic components. This means that they use the dual-branch network architecture proposed in this paper, but with the replacement of the ResBlock in DB-ResNet with the basic structure of networks such as VGG, InceptionNet, and DenseNet.

Table 6 shows the quantification results for the different types of segmentation methods. The results are in the format of “mean ± standard deviation”. To ensure the fairness of the comparison, the methods compared with DB-ResNet in Table 6, the conditions of the experiments are consistent with DB-ResNet including boundary-based sampling strategy, central intensity-pooling layer and post-processing methods. According to the experimental results shown in Table 6, the proposed method is superior to the existing segmentation methods.

Table 7 shows the quantification results of several segmentation methods of the same architecture but with different components. The results are also shown in the format of “mean ± standard deviation”. To achieve a fair comparison, in Table 7, except for the basic components, the other testing conditions are the same. By comparing the experimental results in rows 2 to 8 in Table 7, we can conclude that the DB-ResNet performs the best.

To allow a visual comparison of different approaches, the segmentation results are given in Fig. 6. We demonstrated six representative nodules for visual comparison from the LIDC-IDRI testing set. Notations L1 to L6 shown in Fig. 6 correspond to calcific nodule, juxtalesural nodule, ground-glass opacity nodule, cavitary nodule, isolated nodule, and small nodule less than 6 mm in diameter, respectively. With the visual comparison, it can be seen that the overall performance of the FCN-UNet and MV-CNN methods is slightly inferior to other methods, especially for cavitary nodules and GGO nodules. For isolated nodules, MC-CNN and MCROI-CNN methods performed slightly worse. MCROI-CNN and Cascaded-CNN methods are slightly less effective for juxtalesural

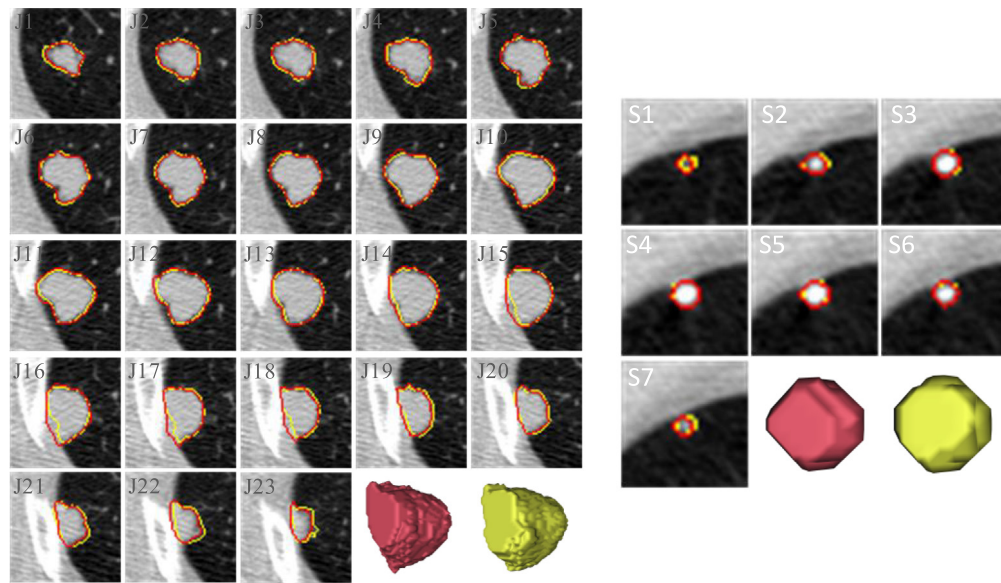


Fig. 7. Segmentation results of DB-ResNet on juxtaleural nodule (J1-L23) and small nodule with a diameter of 4.8 mm (S1-S7) from the LIDC-IDRI testing set. The yellow and red contours represent the segmentation results of DB-ResNet and the ground truth, respectively. The yellow volume data and the red volume data correspond to the 3-D renderings of the DB-ResNet and the ground truth, respectively. The number in the upper left corner of each image represents the slice number where the nodule is located.

Table 5

In the LIDC-IDRI testing sets, DSCs and ASDs for nodules attached, non-attached, less than 6 mm and more than 6 mm in diameter.

	LIDC-IDRI testing set		LIDC-IDRI testing set	
	Attached (n=131)	Non-attached (n=413)	Diameter < 6 mm (n=241)	Diameter ≥ 6 mm (n=303)
DSC (%)	81.79	83.04	79.97	84.94
ASD (mm)	0.25	0.17	0.16	0.21

Table 6

Mean ± standard deviation of the results for various segmentation methods. The best performance is indicated in bold font.

Network architecture	DSC (%)	ASD (mm)	SEN (%)	PPV (%)
FCN-UNet [47]	77.84 ± 21.74	1.79 ± 7.52	77.98 ± 24.52	82.52 ± 21.55
CF-CNN [22]	78.55 ± 12.49	0.27 ± 0.35	86.01 ± 15.22	75.79 ± 14.73
MC-CNN [42]	77.51 ± 11.40	0.29 ± 0.31	88.83 ± 12.34	71.42 ± 14.78
MV-CNN [58]	75.89 ± 12.99	0.31 ± 0.39	87.16 ± 12.91	70.81 ± 17.57
MV-DCNN [43]	77.85 ± 12.94	0.33 ± 0.36	86.96 ± 15.73	77.33 ± 13.26
MCROI-CNN [59]	77.01 ± 12.93	0.30 ± 0.35	85.45 ± 15.97	73.52 ± 14.62
Cascaded-CNN [57]	79.83 ± 10.91	0.26 ± 0.34	86.86 ± 13.35	76.14 ± 13.46
DB-ResNet	82.74 ± 10.19	0.19 ± 0.21	89.35 ± 11.79	79.64 ± 13.34

Table 7

Mean ± standard deviation of quantitative results of segmentation methods using different basic network architectures. The best performance is indicated in the bold font.

Network architecture	DSC (%)	ASD (mm)	SEN (%)	PPV (%)
DB-VGG [60]	80.30 ± 11.34	0.26 ± 0.45	85.40 ± 13.27	78.69 ± 14.49
DB-GoogLeNet [61]	80.61 ± 10.38	0.23 ± 0.29	86.51 ± 12.76	78.03 ± 13.78
DB-Inception-V3 [62]	81.90 ± 10.61	0.22 ± 0.34	87.74 ± 13.57	79.51 ± 13.53
DB-Inception-V4 [63]	80.68 ± 12.40	0.26 ± 0.45	84.67 ± 15.44	80.07 ± 14.55
DB-DenseNet [64]	80.52 ± 11.13	0.24 ± 0.32	86.44 ± 13.95	77.98 ± 13.83
DB-ResDenseNet [65]	79.08 ± 12.27	0.26 ± 0.31	87.58 ± 14.87	75.27 ± 14.55
DB-ResNet	82.74 ± 10.19	0.19 ± 0.21	89.35 ± 11.79	79.64 ± 13.34

nodules. For central calcified nodules, the segmentation results of the MV-DCNN method are incomplete. For small nodules and cavitary nodules, CF-CNN and Cascaded-CNN methods are less adaptable. In contrast, DB-ResNet is still robust when it segments these nodules. This comparison illustrates its significant feature learning capability.

Fig. 7 further shows multiple segmented slices of juxtaleural nodules and small nodules from the LIDC-IDRI testing set with the application of the DB-ResNet. This comparison indicates that

the segmentation results of the DB-ResNet have a large overlap with the ground truth contours.

6. Conclusion

In this study, we proposed a DB-ResNet model for lung nodule segmentation. The model extracts features through dual-branch networks. By comparing with the existing lung nodule segmentation methods, our method showed encouraging accuracy in the

lung nodule segmentation task, and the DSC of 82.74% for the LIDC-IDRI dataset. Especially, the DB-ResNet model can successfully segment challenging cases such as juxta-pleural nodules and small nodules.

In future work, we plan to develop a lung nodule detection algorithm based on the DSSD (deconvolutional single shot detector) network architecture, and then combine it with our method to implement a fully automated segmentation system of the lung nodule.

Declaration of competing interest

No author associated with this paper has disclosed any potential or pertinent conflicts which may be perceived to have impending conflict with this work. For full disclosure statements refer to <https://doi.org/10.1016/j.asoc.2019.105934>.

Acknowledgments

This work is supported by the National Key Research and Development Program of China (Grant No. 2017YFC0112804) and the National Natural Science Foundation of China (Grant No. 81671768). The authors acknowledge the National Cancer Institute and the Foundation for the National Institutes of Health and their critical role in the creation of the publicly available LIDC-IDRI Database for this study.

Appendix A. Supplementary data

Supplementary material related to this article can be found online at <https://doi.org/10.1016/j.asoc.2019.105934>.

References

- [1] R.L. Siegel, K.D. Miller, A. Jemal, Cancer statistics 2017, *CA, Cancer J. Clin.* 67 (2017) 7–30, <http://dx.doi.org/10.3322/caac.21387>.
- [2] H.J.W.L. Aerts, E.R. Velazquez, R.T.H. Leijenaar, C. Parmar, P. Grossmann, S. Carvalho, J. Bussink, R. Monshouwer, B. Haibe-Kains, D. Rietveld, F. Hoebbers, M.M. Rietbergen, C.R. Leemans, A. Dekker, J. Quackenbush, R.J. Gillies, P. Lambin, Decoding tumour phenotype by noninvasive imaging using a quantitative radiomics approach, *Nature Commun.* 5 (2014) 4006, <http://dx.doi.org/10.1038/ncomms5006>.
- [3] H. MacMahon, J.H.M. Austin, G. Gamsu, C.J. Herold, J.R. Jett, D.P. Naidich, E.F. Patz, S.J. Swensen, Guidelines for management of small pulmonary nodules detected on CT scans: A statement from the Fleischner society, *Radiology* 237 (2005) 395–400, <http://dx.doi.org/10.1148/radiol.2372041887>.
- [4] A.P. Reeves, A.B. Chan, D.F. Yankelevitz, C.I. Henschke, B. Kressler, W.J. Kostis, On measuring the change in size of pulmonary nodules, *IEEE Trans. Med. Imaging* 25 (2006) 435–450, <http://dx.doi.org/10.1109/TMI.2006.871548>.
- [5] T. Kubota, A.K. Jerebko, M. Dewan, M. Salganicoff, A. Krishnan, Segmentation of pulmonary nodules of various densities with morphological approaches and convexity models, *Med. Image Anal.* 15 (2011) 133–154, <http://dx.doi.org/10.1016/j.media.2010.08.005>.
- [6] B.C. Lassen, C. Jacobs, J.-M. Kuhnigk, B. van Ginneken, E.M. van Rikxoort, Robust semi-automatic segmentation of pulmonary subsolid nodules in chest computed tomography scans, *Phys. Med. Biol.* 60 (2015) 1307–1323, <http://dx.doi.org/10.1088/0031-9155/60/3/1307>.
- [7] A.A. Farag, H.E.A.E. Munim, J.H. Graham, A.A. Farag, A novel approach for lung nodules segmentation in chest CT using level sets, *IEEE Trans. Image Process.* 22 (2013) 5202–5213, <http://dx.doi.org/10.1109/TIP.2013.2282899>.
- [8] J. Zhao, G. Ji, Y. Xia, X. Zhang, Cavitary nodule segmentation in computed tomography images based on self-generating neural networks and particle swarm optimisation, *IJBIC* 7 (2015) 62–67, <http://dx.doi.org/10.1504/IJBIC.2015.067999>.
- [9] S. Diciotti, S. Lombardo, M. Falchini, G. Picozzi, M. Mascalchi, Automated segmentation refinement of small lung nodules in CT scans by local shape analysis, *IEEE Trans. Biomed. Eng.* 58 (2011) 3418–3428, <http://dx.doi.org/10.1109/TBME.2011.2167621>.
- [10] T. Messay, R.C. Hardie, S.K. Rogers, A new computationally efficient CAD system for pulmonary nodule detection in CT imagery, *Med. Image Anal.* 14 (2010) 390–406, <http://dx.doi.org/10.1016/j.media.2010.02.004>.
- [11] J. Dehmshki, H. Amin, M. Valdivieso, X. Ye, Segmentation of pulmonary nodules in thoracic CT scans: A region growing approach, *IEEE Trans. Med. Imaging* 27 (2008) 467–480, <http://dx.doi.org/10.1109/TMI.2007.907555>.
- [12] X. Ye, G. Beddoe, G.G. Slabaugh, Automatic graph cut segmentation of lesions in CT using mean shift superpixels, *Int. J. Biomed. Imaging* 2010 (2010) 983963:1–983963:14, <http://dx.doi.org/10.1155/2010/983963>.
- [13] T. Messay, R.C. Hardie, T.R. Tuinstra, Segmentation of pulmonary nodules in computed tomography using a regression neural network approach and its application to the lung image database consortium and image database resource initiative dataset, *Med. Image Anal.* 22 (2015) 48–62, <http://dx.doi.org/10.1016/j.media.2015.02.002>.
- [14] M. Keshani, Z. Azimifar, F. Tajeripour, R. Boostani, Lung nodule segmentation and recognition using SVM classifier and active contour modeling: A complete intelligent system, *Comput. Biol. Med.* 43 (2013) 287–300, <http://dx.doi.org/10.1016/j.combiomed.2012.12.004>.
- [15] J. Ding, A. Li, Z. Hu, L. Wang, Accurate pulmonary nodule detection in computed tomography images using deep convolutional neural networks, in: M. Descoteaux, L. Maier-Hein, A. Franz, P. Jannin, D.L. Collins, S. Duchesne (Eds.), *Medical Image Computing and Computer-Assisted Intervention – MICCAI 2017*, Springer International Publishing, Cham, 2017, pp. 559–567.
- [16] Q. Dou, H. Chen, L. Yu, J. Qin, P.A. Heng, Multilevel contextual 3-d CNNs for false positive reduction in pulmonary nodule detection, *IEEE Trans. Biomed. Eng.* 64 (2017) 1558–1567, <http://dx.doi.org/10.1109/TBME.2016.2613502>.
- [17] S. Pereira, A. Pinto, V. Alves, C.A. Silva, Brain tumor segmentation using convolutional neural networks in MRI images, *IEEE Trans. Med. Imaging* 35 (2016) 1240–1251, <http://dx.doi.org/10.1109/TMI.2016.2538465>.
- [18] A. Krizhevsky, I. Sutskever, G.E. Hinton, Imagenet classification with deep convolutional neural networks, in: *Advances in Neural Information Processing Systems 25: 26th Annual Conference on Neural Information Processing Systems 2012 Proceedings of a Meeting Held December 3–6, 2012, Lake Tahoe*, 2012, pp. 1106–1114, <http://papers.nips.cc/paper/4824-imagenet-classification-with-deep-convolutional-neural-networks>.
- [19] P. Moeskops, M.A. Viergever, A.M. Mendrik, L.S. de Vries, M.J.N.L. Benders, I. Išgum, Automatic segmentation of MR brain images with a convolutional neural network, *IEEE Trans. Med. Imaging* 35 (2016) 1252–1261, <http://dx.doi.org/10.1109/TMI.2016.2548501>.
- [20] S. Valverde, A. Oliver, E. Roura, S. González-Villà, D. Pareto, J.C. Vilanova, L. Ramió-Torrentà, À. Rovira, X. Lladó, Automated tissue segmentation of MR brain images in the presence of white matter lesions, *Med. Image Anal.* 35 (2017) 446–457, <http://dx.doi.org/10.1016/j.media.2016.08.014>.
- [21] W. Zhang, R. Li, H. Deng, L. Wang, W. Lin, S. Ji, D. Shen, Deep convolutional neural networks for multi-modality isointense infant brain image segmentation, *Neuroimage* 108 (2015) 214–224, <http://dx.doi.org/10.1016/j.neuroimage.2014.12.061>.
- [22] S. Wang, M. Zhou, Z. Liu, Z. Liu, D. Gu, Y. Zang, D. Dong, O. Gevaert, J. Tian, Central focused convolutional neural networks: Developing a data-driven model for lung nodule segmentation, *Med. Image Anal.* 40 (2017) 172–183, <http://dx.doi.org/10.1016/j.media.2017.06.014>.
- [23] W.J. Kostis, A.P. Reeves, D.F. Yankelevitz, C.I. Henschke, Three-dimensional segmentation and growth-rate estimation of small pulmonary nodules in helical CT images, *IEEE Trans. Med. Imaging* 22 (2003) 1259–1274, <http://dx.doi.org/10.1109/TMI.2003.817785>.
- [24] D. Sargent, S.Y. Park, Semi-automatic 3D lung nodule segmentation in CT using dynamic programming, in: *Proc. SPIE*, 2017, <http://dx.doi.org/10.1117/12.2254575>.
- [25] J.M. Kuhnigk, V. Dicken, L. Bornemann, A. Bakai, D. Wormanns, S. Krass, H.O. Peitgen, Morphological segmentation and partial volume analysis for volumetry of solid pulmonary lesions in thoracic CT scans, *IEEE Trans. Med. Imaging* 25 (2006) 417–434, <http://dx.doi.org/10.1109/TMI.2006.871547>.
- [26] T.F. Chan, L.A. Vese, Active contours without edges, *IEEE Trans. Image Process.* 10 (2001) 266–277, <http://dx.doi.org/10.1109/83.902291>.
- [27] E.E. Nithila, S.S. Kumar, Segmentation of lung nodule in CT data using active contour model and fuzzy C-mean clustering, *Alexandria Eng. J.* 55 (2016) 2583–2588, <http://dx.doi.org/10.1016/j.aej.2016.06.002>.
- [28] J. Wang, H. Guo, Automatic approach for lung segmentation with juxta-pleural nodules from thoracic CT based on contour tracing and correction, *Comput. Math. Methods Med.* 2016 (2016) 2962047:1–2962047:13, <http://dx.doi.org/10.1155/2016/2962047>.
- [29] P.P.R. Filho, A.C. da Silva Barros, J.S. Almeida, J.P.C. Rodrigues, V.H.C. de Albuquerque, A new effective and powerful medical image segmentation algorithm based on optimum path snakes, *Appl. Soft Comput.* 76 (2019) 649–670, <http://dx.doi.org/10.1016/j.asoc.2018.10.057>.
- [30] Y. Boykov, V. Kolmogorov, An experimental comparison of min-cut/max-flow algorithms for energy minimization in vision, *IEEE Trans. Pattern Anal. Mach. Intell.* 26 (2004) 1124–1137, <http://dx.doi.org/10.1109/TPAMI.2004.60>.
- [31] S. Mukherjee, X. Huang, R.R. Bhagalia, Lung nodule segmentation using deep learned prior based graph cut, in: *2017 IEEE 14th Int. Symp. Biomed. Imaging, ISBI 2017*, 2017, pp. 1205–1208, <http://dx.doi.org/10.1109/ISBI.2017.7950733>.

- [32] L. Lu, A. Barbu, M. Wolf, J. Liang, M. Salganicoff, D. Comaniciu, Accurate polyp segmentation for 3D CT colonography using multi-staged probabilistic binary learning and compositional model, in: 2008 IEEE Conf. Comput. Vis. Pattern Recognit., 2008, pp. 1–8, <http://dx.doi.org/10.1109/CVPR.2008.4587423>.
- [33] L. Lu, J. Bi, M. Wolf, M. Salganicoff, Effective 3D object detection and regression using probabilistic segmentation features in CT images, in: CVPR 2011, 2011, pp. 1049–1056, <http://dx.doi.org/10.1109/CVPR.2011.5995359>.
- [34] S. Mukhopadhyay, A segmentation framework of pulmonary nodules in lung CT images, *J. Digit. Imaging* 29 (2016) 86–103, <http://dx.doi.org/10.1007/s10278-015-9801-9>.
- [35] S. Shen, A.A.T. Bui, J. Cong, W. Hsu, An automated lung segmentation approach using bidirectional chain codes to improve nodule detection accuracy, *Comput. Biol. Med.* 57 (2015) 139–149, <http://dx.doi.org/10.1016/j.compbiomed.2014.12.008>.
- [36] L. Lu, P. Devarakota, S. Vikal, D. Wu, Y. Zheng, M. Wolf, Computer aided diagnosis using multilevel image features on large-scale evaluation, in: B. Menze, G. Langs, A. Montillo, M. Kelm, H. Müller, Z. Tu (Eds.), *Medical Computer Vision. Large Data in Medical Imaging*, Springer International Publishing, Cham, 2014, pp. 161–174.
- [37] D. Wu, L. Lu, J. Bi, Y. Shinagawa, K. Boyer, A. Krishnan, M. Salganicoff, Stratified learning of local anatomical context for lung nodules in CT images, in: 2010 IEEE Comput. Soc. Conf. Comput. Vis. Pattern Recognit., 2010, pp. 2791–2798, <http://dx.doi.org/10.1109/CVPR.2010.5540008>.
- [38] Y. Hu, P.G. Menon, A neural network approach to lung nodule segmentation, in: *Proc. SPIE*, 2016, <http://dx.doi.org/10.1117/12.2217291>.
- [39] J. Jung, H. Hong, J.M. Goo, Ground-glass nodule segmentation in chest CT images using asymmetric multi-phase deformable model and pulmonary vessel removal, *Comput. Biol. Med.* 92 (2018) 128–138, <http://dx.doi.org/10.1016/j.compbiomed.2017.11.013>.
- [40] L. Gonçalves, J. Novo, A. Campilho, Hessian based approaches for 3D lung nodule segmentation, *Expert Syst. Appl.* 61 (2016) 1–15, <http://dx.doi.org/10.1016/j.eswa.2016.05.024>.
- [41] W. Gao, Z.-H. Zhou, Dropout rademacher complexity of deep neural networks, *Sci. China Inf. Sci.* 59 (2016) 72104, <http://dx.doi.org/10.1007/s11432-015-5470-z>.
- [42] W. Shen, M. Zhou, F. Yang, D. Yu, D. Dong, C. Yang, Y. Zang, J. Tian, Multi-crop convolutional neural networks for lung nodule malignancy suspiciousness classification, *Pattern Recognit.* 61 (2017) 663–673, <http://dx.doi.org/10.1016/j.patcog.2016.05.029>.
- [43] S. Wang, M. Zhou, O. Gevaert, Z. Tang, D. Dong, Z. Liu, J. Tian, A multi-view deep convolutional neural networks for lung nodule segmentation, in: 2017 39th Annu. Int. Conf. IEEE Eng. Med. Biol. Soc., 2017, pp. 1752–1755, <http://dx.doi.org/10.1109/EMBC.2017.8037182>.
- [44] X. Zhao, W. Sun, W. Qian, S. Qi, J. Sun, B. Zhang, Z. Yang, Fine-grained lung nodule segmentation with pyramid deconvolutional neural network, in: *Proc. SPIE*, 2019, <http://dx.doi.org/10.1117/12.2512609>.
- [45] X. Huang, W. Sun, T.-L. (Bill) Tseng, C. Li, W. Qian, Fast and fully-automated detection and segmentation of pulmonary nodules in thoracic CT scans using deep convolutional neural networks, *Comput. Med. Imaging Graph.* 74 (2019) 25–36, <http://dx.doi.org/10.1016/j.compmedimag.2019.02.003>.
- [46] J. Long, E. Shelhamer, T. Darrell, Fully convolutional networks for semantic segmentation, in: 2015 IEEE Conf. Comput. Vis. Pattern Recognit., 2015, pp. 3431–3440, <http://dx.doi.org/10.1109/CVPR.2015.7298965>.
- [47] O. Ronneberger, P. Fischer, T. Brox, U-net: Convolutional networks for biomedical image segmentation, in: N. Navab, J. Hornegger, W.M. Wells, A.F. Frangi (Eds.), *Medical Image Computing and Computer-Assisted Intervention – MICCAI 2015*, Springer International Publishing, Cham, 2015, pp. 234–241.
- [48] Ö. Çiçek, A. Abdulkadir, S.S. Lienkamp, T. Brox, O. Ronneberger, 3D U-net: Learning dense volumetric segmentation from sparse annotation, in: S. Ourselin, L. Joskowicz, M.R. Sabuncu, G.H. Unal, W. Wells (Eds.), *Medical Image Computing and Computer-Assisted Intervention – MICCAI 2016*, Springer International Publishing, Cham, 2016, pp. 424–432.
- [49] K. He, X. Zhang, S. Ren, J. Sun, Deep residual learning for image recognition, in: 2016 IEEE Conf. Comput. Vis. Pattern Recognit., 2016, pp. 770–778, <http://dx.doi.org/10.1109/CVPR.2016.90>.
- [50] S. Ioffe, C. Szegedy, Batch normalization: Accelerating deep network training by reducing internal covariate shift, in: *Proceedings of the 32nd International Conference on Machine Learning, ICML 2015, Lille, France, 6–11 July 2015*, 2015, pp. 448–456, <http://jmlr.org/proceedings/papers/v37/loffe15.html>.
- [51] K. He, X. Zhang, S. Ren, J. Sun, Delving deep into rectifiers: Surpassing human-level performance on imagenet classification, in: 2015 IEEE Int. Conf. Comput. Vis., 2015, pp. 1026–1034.
- [52] L. Wang, Y. Yang, R. Min, S. Chakradhar, Accelerating deep neural network training with inconsistent stochastic gradient descent, *Neural Netw.* 93 (2017) 219–229, <http://dx.doi.org/10.1016/j.neunet.2017.06.003>.
- [53] R. Caruana, S. Lawrence, C.L. Giles, Overfitting in neural nets: Back-propagation, conjugate gradient, and early stopping, in: *Advances in Neural Information Processing Systems 13*, Papers from Neural Information Processing Systems (NIPS) 2000, Denver, CO, USA, 2000, pp. 402–408, <http://papers.nips.cc/paper/1895-overfitting-in-neural-nets-backpropagation-conjugate-gradient-and-early-stopping>.
- [54] S.G. Armato, G. McLennan, L. Bidaut, M.F. McNitt-Gray, C.R. Meyer, A.P. Reeves, B. Zhao, D.R. Aberle, C.I. Henschke, E.A. Hoffman, E.A. Kazerooni, H. MacMahon, E.J.R. Van Beeke, D. Yankelevitz, A.M. Biancardi, P.H. Bland, M.S. Brown, R.M. Engelmann, G.E. Laderach, D. Max, R.C. Pais, D.P.Y. Qing, R.Y. Roberts, A.R. Smith, A. Starkey, P. Batrah, P. Caligiuri, A. Farooqi, G.W. Gladish, C.M. Jude, R.F. Munden, I. Petkovska, L.E. Quint, L.H. Schwartz, B. Sundaram, L.E. Dodd, C. Fenimore, D. Gur, N. Petrick, J. Freymann, J. Kirby, B. Hughes, A. Vande Castele, S. Gupta, M. Sallamm, M.D. Heath, M.H. Kuhn, E. Dharaiya, R. Burns, D.S. Fryd, M. Salganicoff, V. Anand, U. Shreter, S. Vastagh, B.Y. Croft, The lung image database consortium (LIDC) and image database resource initiative (IDRI): a completed reference database of lung nodules on CT scans, *Med. Phys.* 38 (2011) 915–931, <http://dx.doi.org/10.1118/1.3528204>.
- [55] A.A.A. Setio, F. Ciompi, G. Litjens, P. Gerke, C. Jacobs, S.J. van Riel, M.M.W. Wille, M. Naqibullah, C.I. Sánchez, B. van Ginneken, Pulmonary nodule detection in CT images: False positive reduction using multi-view convolutional networks, *IEEE Trans. Med. Imaging* 35 (2016) 1160–1169, <http://dx.doi.org/10.1109/TMI.2016.2536809>.
- [56] A.A.A. Setio, A. Traverso, T. de Bel, M.S.N. Berens, C. van den Bogaard, P. Cerello, H. Chen, Q. Dou, M.E. Fantacci, B. Geurts, R. van der Gugten, P.A. Heng, B. Jansen, M.M.J. de Kaste, V. Kotov, J.Y.-H. Lin, J.T.M.C. Manders, A. Sónora Mengana, J.C. García-Naranjo, E. Papavasileiou, M. Prokop, M. Saletta, C.M. Schaefer-Prokop, E.T. Scholten, L. Scholten, M.M. Snoeren, E.L. Torres, J. Vandemeulebroucke, N. Walasek, G.C.A. Zuidhof, B. van Ginneken, C. Jacobs, Validation, comparison, And combination of algorithms for automatic detection of pulmonary nodules in computed tomography images: The luna16 challenge, *Med. Image Anal.* 42 (2017) 1–13, <http://dx.doi.org/10.1016/j.media.2017.06.015>.
- [57] M. Havaei, A. Davy, D. Warde-Farley, A. Biard, A.C. Courville, Y. Bengio, C. Pal, P.-M. Jodoin, H. Larochelle, Brain tumor segmentation with deep neural networks, *Med. Image Anal.* 35 (2017) 18–31, <http://dx.doi.org/10.1016/j.media.2016.05.004>.
- [58] G. Kang, K. Liu, B. Hou, N. Zhang, 3d multi-view convolutional neural networks for lung nodule classification, *PLoS One* 12 (2017) e0188290, <http://dx.doi.org/10.1371/journal.pone.0188290>.
- [59] W. Sun, B. Zheng, W. Qian, Automatic feature learning using multichannel ROI based on deep structured algorithms for computerized lung cancer diagnosis, *Comput. Biol. Med.* 89 (2017) 530–539, <http://dx.doi.org/10.1016/j.compbiomed.2017.04.006>.
- [60] K. Simonyan, A. Zisserman, Very deep convolutional networks for large-scale image recognition, 2014, CoRR. abs/1409.1 <http://arxiv.org/abs/1409.1556>.
- [61] C. Szegedy, W. Liu, Y. Jia, P. Sermanet, S. Reed, D. Anguelov, D. Erhan, V. Vanhoucke, A. Rabinovich, Going deeper with convolutions, in: 2015 IEEE Conf. Comput. Vis. Pattern Recognit., 2015, pp. 1–9, <http://dx.doi.org/10.1109/CVPR.2015.7298594>.
- [62] C. Szegedy, V. Vanhoucke, S. Ioffe, J. Shlens, Z. Wojna, Rethinking the inception architecture for computer vision, in: 2016 IEEE Conf. Comput. Vis. Pattern Recognit., 2016, pp. 2818–2826, <http://dx.doi.org/10.1109/CVPR.2016.308>.
- [63] C. Szegedy, S. Ioffe, V. Vanhoucke, A.A. Alemi, Inception-v4, inception-resnet and the impact of residual connections on learning, in: *Proceedings of the Thirty-First AAAI Conference on Artificial Intelligence*, February 4–9, 2017, San Francisco, California, USA, 2017, pp. 4278–4284, <http://aaai.org/ocs/index.php/AAAI/AAAI17/paper/view/14806>.
- [64] G. Huang, Z. Liu, L. v. d. Maaten, K.Q. Weinberger, Densely connected convolutional networks, in: 2017 IEEE Conf. Comput. Vis. Pattern Recognit., 2017, pp. 2261–2269, <http://dx.doi.org/10.1109/CVPR.2017.243>.
- [65] Y. Zhang, Y. Tian, Y. Kong, B. Zhong, Y. Fu, Residual dense network for image super-resolution, 2018, CoRR. abs/1802.0 <http://arxiv.org/abs/180208797>.